International Journal of Heat and Mass Transfer 255 (2026) 127785

Contents lists available at ScienceDirect

International Journal of Heat and Mass Transfer

journal homepage: www.elsevier.com/locate/ijhmt

Influence of local perforations on heat transfer enhancement in inclined rib turbulators

Dosang Lee [a], Hyung Ju Lee [b], Hyoungsoon Lee [a], Seong Hyuk Lee [a,*]

[a] School of Mechanical Engineering, Chung-Ang University, Seoul 06974, Republic of Korea
[b] Department of Mechanical Engineering, Gangneung-Wonju National University, Wonju-si, Gangwon-do 26403, Republic of Korea

ARTICLE INFO

Keywords:
Local perforation
Turbine rib turbulator
Computational fluid dynamics
Heat transfer
Overall thermal performance factor

ABSTRACT

The present study numerically investigates the influence of tailored local perforations on swirling flows and their influence on heat transfer enhancement in the rib turbulators. Numerical simulations are conducted for various rib inclination angles and perforation positions. The results indicate that ribs inclined at 60° and 30° increase the normalized Nusselt number by approximately 23.2 % and 17.0 %, respectively, and improve the overall thermal performance factor by 11.9 % and 24.5 %, compared to conventional 90° inclined ribs. To further enhance heat transfer performance, ten perforations are applied in parallel with the flow direction at one end of each inclined rib, targeting the local swirling flow. These perforated configurations enhance turbulent mixing and strengthen the vortex structures, improving heat transfer over the bottom surface. For the 60° and 30° inclined ribs, the local perforations increase the normalized Nusselt number by 5.1 % and 4.4 %, respectively, while reducing the normalized friction loss by 1.5 % and 5.7 %, resulting in overall thermal performance improvements of 5.6 % and 6.5 %. In contrast, when perforations are applied at both ends of the 30° inclined ribs, the secondary flow is disrupted, leading to a localized reduction in heat transfer. This configuration yields an approximately 9.2 % lower overall thermal performance factor than the case with ten perforations positioned only at the left end of the 30° inclined ribs.

1. Introduction

The gas turbine plays a crucial role in efficiently converting heat into power, finding widespread application in power generation and propulsion of aircraft and ships. Developing gas turbine engines with improved thermal efficiency and output is essential for reducing fuel consumption and mitigating environmental pollution. The most common approach for enhancing the efficiency and power output of a gas turbine engine is to increase the operating temperature of the turbine [1–3]. Many studies have reported that a mere 50 K increase in turbine entry temperature (TET) can yield a substantial 8–9 % increase in power output and a notable 2–4 % enhancement in cycle efficiency [1]. In pursuit of these gains, the development trajectory of gas turbine engines has shown a distinct focus on elevating the operating temperature of the turbine [1–3]. The operating temperature of turbines will soon approach 2000 K, surpassing the current limit of turbine materials [2]. However, a temperature increase of 30 K beyond the allowable limit for metal blades reduced their lifespan by half [4], indicating that advanced cooling technologies are necessary under higher operating temperatures. To overcome this limitation is crucial for bridging the technical gap between the TET and the maximum permissible material temperature.

Previous works have focused on various interfacial forced convection cooling strategies, utilizing internal cooling air within the blade to enhance the performance and durability of turbines. Internal cooling approaches, such as rib turbulators [5–7], dimpled surfaces [8,9], pin-fin arrays [10,11], and impingement jets [12,13]. Among these techniques, rib turbulators are passive cooling structures integrated into the walls of internal cooling channels within the blade. Due to their simplicity and flexibility in design and size, they are widely applied in the cooling passages of the mid-section of airfoils [2]. When cooling air enters the ribbed channel, flow separation occurs at the edges of the ribs, generating a backward-facing step flow where the shear layer separates, resulting in the flow dividing into recirculation and reattachment regions [14]. The secondary flow induced by rib turbulators is one of the primary factors contributing to heat transfer enhancement in cooling passages, but it also intensifies the pressure drop, thereby reducing cooling performance. Therefore, several studies have investigated the influence of rib geometry on the internal flow structure of the channel to

* Corresponding author.
E-mail address: shlee89@cau.ac.kr (S.H. Lee).

https://doi.org/10.1016/j.ijheatmasstransfer.2025.127785
Received 24 March 2025; Received in revised form 27 July 2025; Accepted 29 August 2025

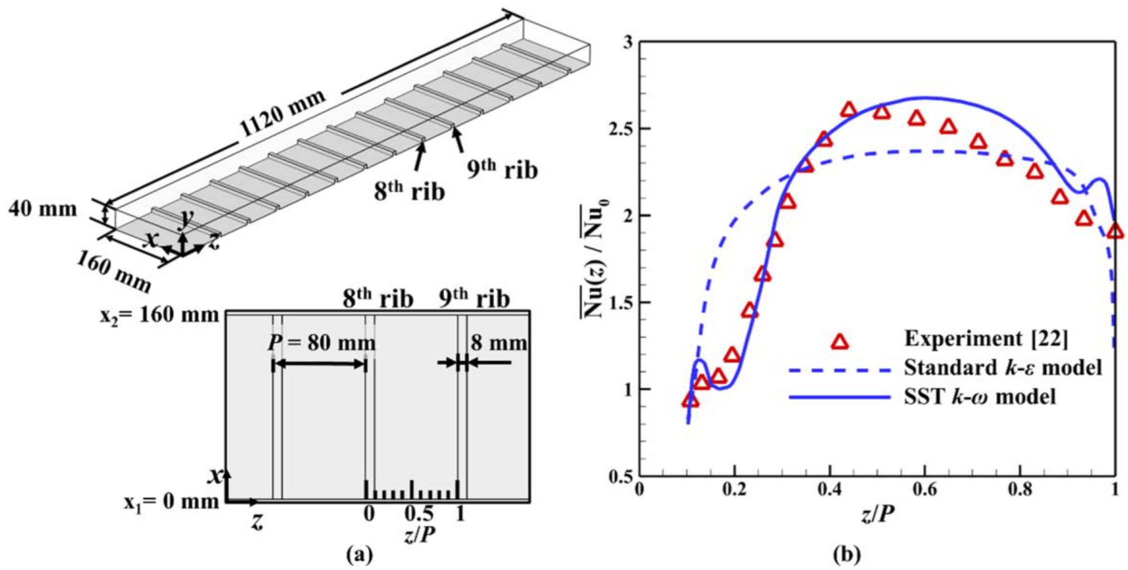

Fig. 1. (a) Schematic of the computational domain used for preliminary validation, and (b) comparison of the spanwise area-averaged Nusselt number between the eighth and ninth ribs using two different turbulence models.

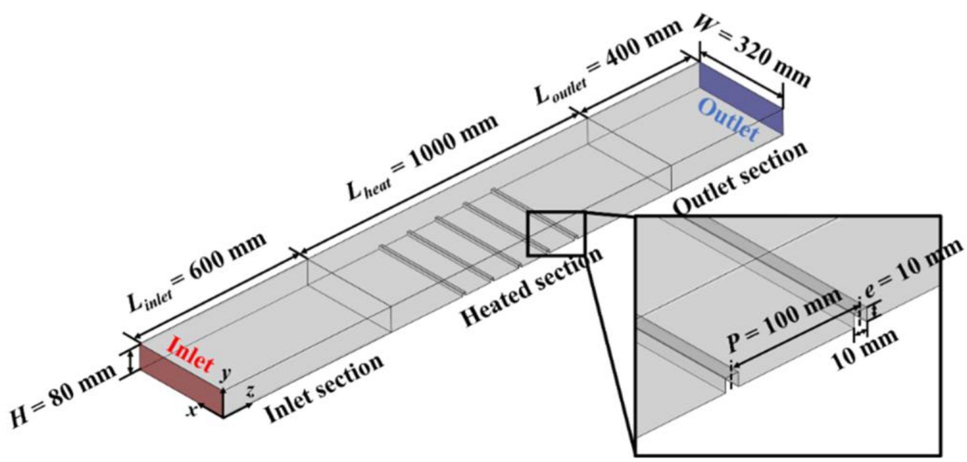

Fig. 2. A schematic of the computational domain.

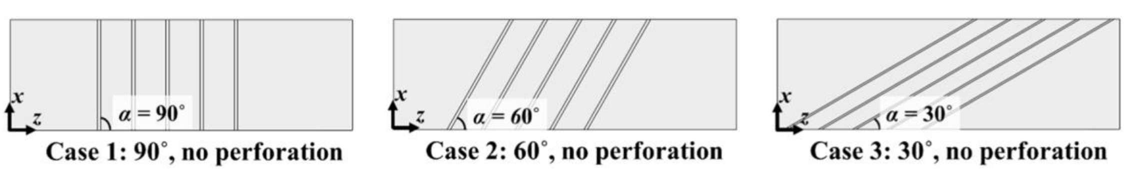

Fig. 3. Configurations of the three different cases without perforations.

Table 1
Properties of air [28].

Property	Value
Density	1.225 kg/m^3
Thermal conductivity	0.0242 W/m·K
Specific heat	1006.43 J/kg·K
Viscosity	1.7894×10^{-5} kg/m·s

enhance heat transfer while minimizing the frictional effects caused by the ribs. Kaewchoothong et al. [15] experimentally investigated the influence of different inclination angles and V-shaped ribs on local heat transfer characteristics and the impact of friction on three-dimensional flow. They found that a rib inclination angle of 30° produces the highest overall thermal performance factor under low friction loss. Also, Yang et al. [16] numerically simulated the effect of varying rib inclination angles at 30°, 45°, 60°, and 90°. They found that cases with inclined ribs show similar secondary flow distribution and enhanced overall thermal performance factors, primarily due to the longitudinal secondary flow downstream.

In recent years, perforated ribs have received significant attention to enhance heat transfer performance while reducing pressure drop [17–19]. Liu et al. [17] also investigated cooling characteristics in a rectangular channel using perforated ribs with inclined holes, ranging from 0° to 45°, and with circular and square hole shapes. It was concluded that the perforations could enhance the overall average

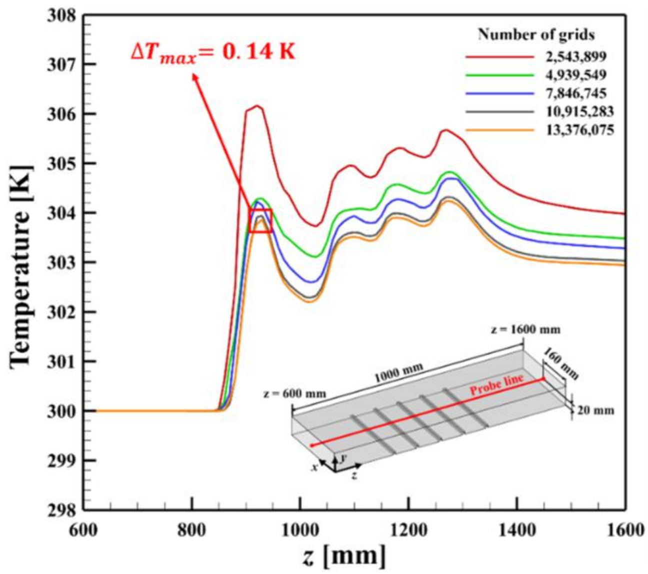

Fig. 4. Grid-independence tests for Case 1.

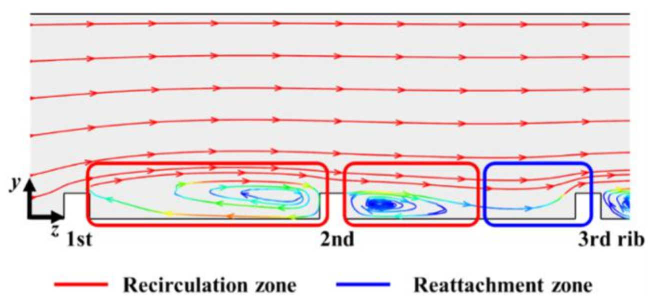

Fig. 5. Flow characteristics, including velocity magnitude and streamlines in the y-z plane at $x = 160$ mm for Case 1.

Nusselt number by mitigating the recirculating flows behind the ribs but creating a local region of low Nusselt numbers on the side opposite the inclination direction. Liu et al. [18] experimentally and numerically investigated the effects of different perforation shapes and intervals on heat transfer and friction. The results demonstrated that perforations mitigated the low heat transfer regions caused by recirculating flows and reduced friction, improving the overall thermal performance factor and the uniformity of the cooling effect. This observation was more pronounced in the cases of round holes with smaller intervals. Qian et al. [19] examined the flow patterns and heat transfer performance when horizontal or upward/downward tilted perforations were applied to vertical ribs through both experimental and numerical methods. They found that the perforations reduced the pressure drop within the channel and improved heat transfer performance. However, both studies exhibited non-uniform heat transfer distribution, showing high heat transfer regions at the leading edge of the inclined ribs and low heat transfer regions at the trailing edge.

According to previous studies, inclined ribs have been shown to enhance heat transfer by generating secondary flows; however, they have also caused pressure drop and non-uniform flow distributions. While perforations can reduce pressure drop and improve flow uniformity, they may weaken the intensity of secondary flow, potentially compromising local heat transfer performance. Unlike the previous approach [17–19], the main objective of this study is to propose a novel method that utilizes tailored localized perforations, specifically designed to induce a local swirling flow, promoting turbulent mixing and enhancing heat transfer in an inclined rib channel. Extensive CFD simulations are conducted to comprehensively analyze the flow characteristics for different arrangements of local perforations and rib inclination angles. Based on numerical insights, a physics-informed configuration is suggested by partially locating perforations on only one side of the inclined ribs, which controls secondary flow and improves overall thermal performance while minimizing disruption in high heat transfer regions.

2. Numerical methods

2.1. Mathematical representation

Numerical simulations were conducted using ANSYS FLUENT (2020 R2) with three-dimensional, turbulent, incompressible, and steady-state assumptions. Radiation heat transfer and the gravitational force were also assumed to be negligible. The present study solves the Reynolds-Averaged Navier–Stokes (RANS) equations with the energy and mass conservation equations, expressed as follows:

$$\frac{\partial(\rho\overline{u}_i)}{\partial x_i} = 0, \tag{1}$$

$$\frac{\partial}{\partial x_i}(\rho\overline{u}_i\overline{u}_j) = -\frac{\partial\overline{p}}{\partial x_i} + \frac{\partial}{\partial x_j}\left[\mu\left(\frac{\partial\overline{u}_i}{\partial x_j} + \frac{\partial\overline{u}_j}{\partial x_i} - \frac{2}{3}\delta_{ij}\frac{\partial\overline{u}_l}{\partial\overline{u}_l}\right)\right] + \frac{\partial}{\partial x_i}\left(-\rho\overline{u'_i u'_j}\right), \tag{2}$$

$$\frac{\partial}{\partial x_i}(\overline{u}_i(\rho E + p)) = \frac{\partial}{\partial x_i}\left(k_{eff}\frac{\partial T}{\partial x_i} + \overline{\tau}_{eff}\cdot\overline{u}_i\right), \tag{3}$$

where ρ, μ, $\overline{u}_i$, and u'_i are the density, dynamic viscosity of the flow, time-averaged velocity, and fluctuating velocity, respectively. In Eq. (3), E is the total energy, k_{eff} is the effective thermal conductivity, and τ_{eff} is the deviatoric stress tensor. This study also utilized the Shear Stress Transport (SST) k–ω model to effectively account for secondary vortical flows and separation behavior, which typically occur near the ribbed channels [17,19–21]. The two equations for the additional turbulent quantities can be expressed by

$$\frac{\partial}{\partial x_i}(\rho k u_i) = \frac{\partial}{\partial x_j}\left(\Gamma_k\frac{\partial k}{\partial x_j}\right)\frac{\partial T}{\partial x_j} + G_k - Y_k, \tag{4}$$

$$\frac{\partial}{\partial x_i}(\rho\omega) + \frac{\partial}{\partial x_i}(\rho\omega u_i) = \frac{\partial}{\partial x_j}\left(\Gamma_\omega\frac{\partial\omega}{\partial x_j}\right) + G_\omega - Y_\omega + D_\omega, \tag{5}$$

where k is turbulent kinetic energy (TKE), ω is the specific dissipation rate, G_k is the generation of k from the mean velocity gradients, G_ω denotes the generation of ω, and D_ω represents the cross-diffusion term. Y_k and Y_ω denote the dissipation of k and ω from turbulence, respectively. For the square channel, the Reynolds number at the inlet was defined as

$$\mathrm{Re} = \frac{\rho u_{inlet} D_h}{\mu}, \tag{6}$$

where D_h is the hydraulic diameter of the channel's inlet and u_{inlet} is the inlet air velocity. The local Nusselt number on the bottom wall of the heated section was calculated as follows:

$$\mathrm{Nu}(x,z) = \frac{q_w D_h}{(T_w(x,z) - T_{avg})\lambda}, \tag{7}$$

Here, $T_w(x, z)$ is the local temperature at the bottom wall, T_{avg} is the average temperature of the air in the heated section, and λ is the thermal conductivity of the air. The average Nusselt number of the heated section is calculated as the area-weighted average of the local Nusselt numbers:

$$\overline{\mathrm{Nu}} = \frac{1}{A}\iint_A \mathrm{Nu}(x,z)\,dx\,dz, \tag{8}$$

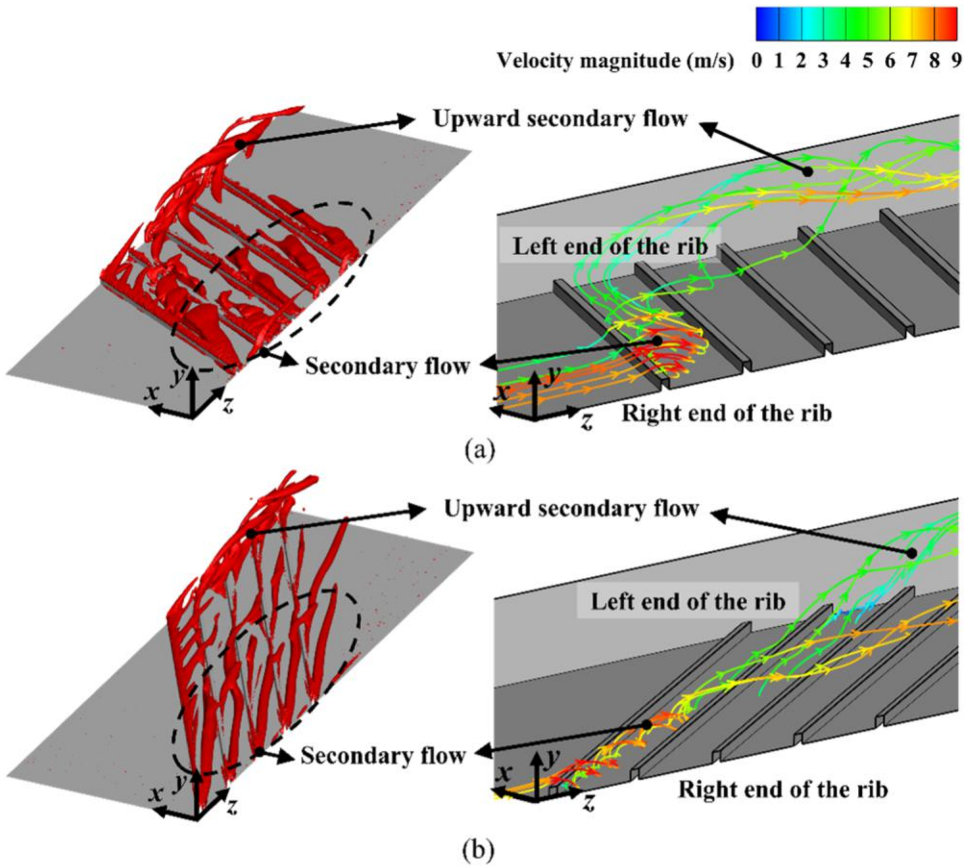

Fig. 6. Secondary flow characteristics including vortical flows, velocity magnitude, and streamlines for (a) Case 2, and (b) Case 3.

where Nu(x, z) is the local Nusselt number. For calculating the overall Nusselt number, A represents the total area of the bottom wall in the heated section. Meanwhile, the friction loss representing the pressure drop within the ribbed channel is expressed by

$$f = \frac{\Delta p}{2\rho u_{inlet}^2} \cdot \frac{D_h}{L_{heat}}, \tag{9}$$

where Δp represents the pressure drop within the channel, calculated as the difference between the area-weighted averages of the pressures at the inlet and outlet of the heated section. To evaluate the performance of the ribbed channel, the normalized overall Nusselt number, $\overline{\mathrm{Nu}}/\mathrm{Nu}_0$, and normalized friction loss, f/f_0, are used. For normalization, the Nusselt number is calculated using the well-known Dittus–Boelter equation (Eq. (10)), whereas the friction loss is determined based on the Blasius correlation (Eq. (11)).

$$\overline{\mathrm{Nu}}_0 = 0.023\mathrm{Re}^{0.8}\mathrm{Pr}^{0.4}, \tag{10}$$

$$f_0 = 0.079\mathrm{Re}^{-0.25}, \tag{11}$$

where Pr represents the Prandtl number. Since the performance of ribbed channels should be analyzed by considering both heat transfer and flow characteristics, the present study employs the overall thermal performance factor, which represents heat transfer performance relative to pressure loss in the channel, to evaluate the cooling performance as expressed by

$$\eta = \frac{\overline{\mathrm{Nu}}/\overline{\mathrm{Nu}}_0}{(f/f_0)^{1/3}}. \tag{12}$$

2.2. Preliminary test for validation

A preliminary test was conducted for validation by comparing the simulation results with experimental data reported in the previous study [22]. Fig. 1(a) presents the configuration used for preliminary simulations, which were performed based on the same geometry and boundary conditions reported in the literature [22]. The computational domain includes a rectangular heated section with dimensions of 1500 mm in length, 160 mm in width, and 40 mm in thickness, incorporating rib structures with a height of 8 mm mounted on the bottom wall. The channel aspect ratio is 4:1, and the corresponding hydraulic diameter is 64 mm. A uniform velocity profile was imposed at the channel inlet, corresponding to a Reynolds number of 42,500, with an inlet temperature of 300 K. The outlet boundary condition was set to a static pressure condition with zero-gauge pressure. All smooth walls were assumed to be adiabatic with no-slip conditions. A uniform heat flux of 1000 W/m^2 was applied to the bottom wall. To assess the predictive accuracy of turbulence models, numerical results obtained using the SST k–ω and standard k–ε models were compared with experimental data [22]. The spanwise-averaged Nusselt numbers estimated between the eighth and ninth ribs were compared with the experimental results, as shown in Fig. 1(b). The spanwise area-averaged Nusselt number was calculated as follows:

$$\overline{\mathrm{Nu}}(z) = \frac{1}{x_2 - x_1}\int_{x_1}^{x_2} \mathrm{Nu}(x,z)\,dx \qquad (x_1 = 0\,\mathrm{mm},\ x_2 = 160\,\mathrm{mm},\ y = 0,\ 0 \le z/P \le 1), \tag{13}$$

where Nu(x, z) is the local Nusselt number. The results indicate that the SST k–ω model exhibits better agreement with the experimental data than the standard k–ε model. As reported in previous studies [23,24],

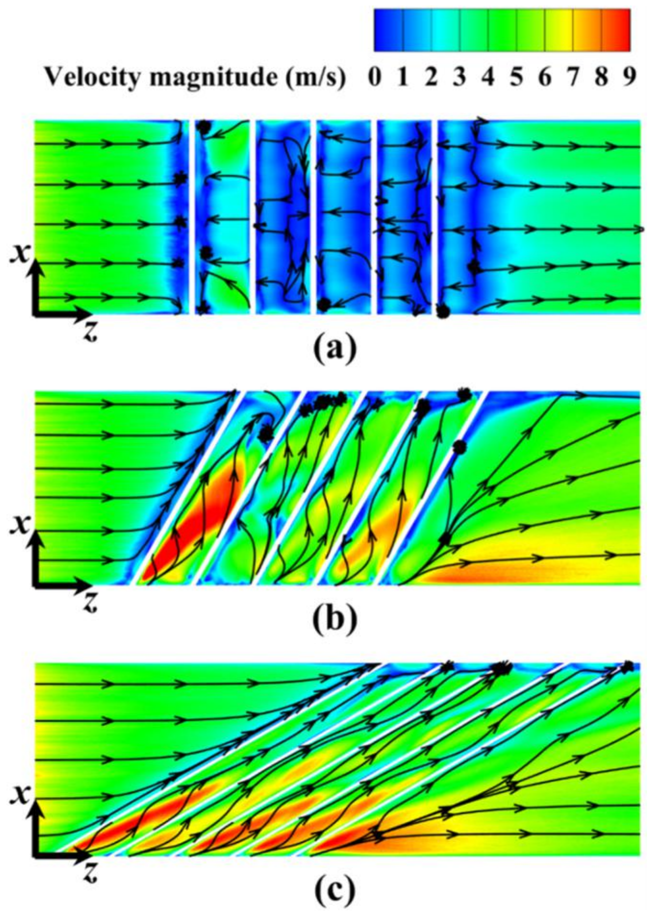

Fig. 7. The predicted distributions of velocity magnitude on the x–z plane at y = 1 mm for (a) Case 1, (b) Case 2, and (c) Case 3.

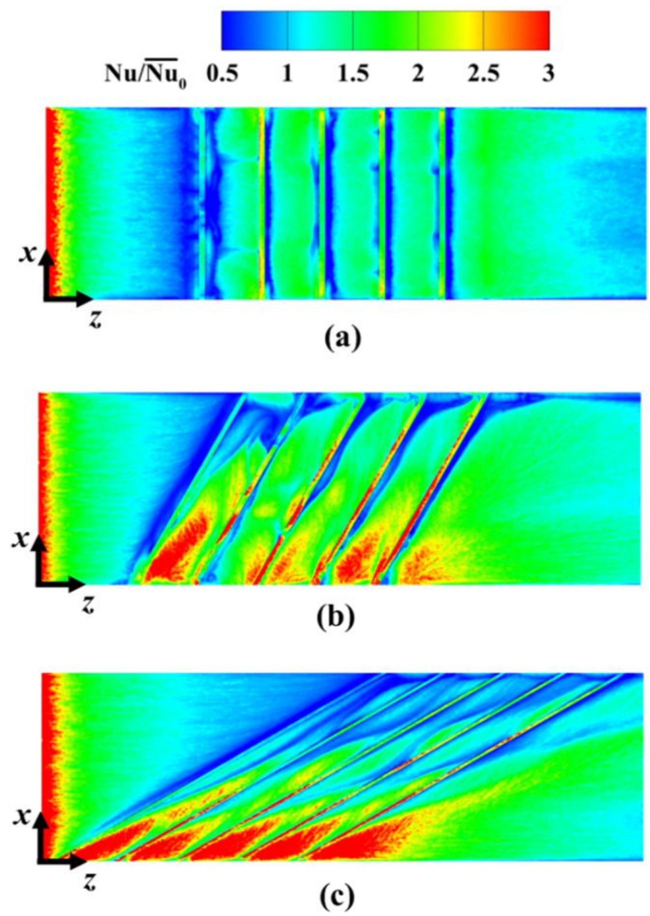

Fig. 8. Normalized Nusselt number distributions at the bottom surface of the heated section in (a) Case 1, (b) Case 2, and (c) Case 3.

the SST k–ω model more effectively resolves near-wall turbulence, providing more accurate predictions of rib-induced secondary flows. Based on this result, the present study employed the SST k–ω model for all cases to investigate the effects of tailored local perforations on swirling flows and their influence on heat transfer characteristics.

2.3. Computational domain and boundary conditions

Based on the preliminary validation described above, the present study employed the SST k–ω model, which demonstrated better agreement with experimental data than the standard k–ε model. Numerical case studies were subsequently conducted for various inclined rib angles and local perforation configurations using a reference configuration consisting of a simplified rectangular channel with five rib turbulators on the heated section, as illustrated in Fig. 2, which has been widely used in the literature [5,17,18,25,26] for computational simplicity. The cross-section of the channel was constructed to have a height, H, of 80 mm and a width, W, of 320 mm, with an aspect ratio, W/H, of 4. The hydraulic diameter of the rectangular channel is given by $D_h = 2WH/(W+H)$ and is calculated to be 128 mm. The rectangular channel consists of three sections: the inlet section, the heated section, and the outlet section, each with a length of 600 mm, 1000 mm, and 400 mm, respectively. The inlet section length is determined to achieve fully developed turbulent flow [27], and the outlet section is placed after the heated section to reduce the incidence of reverse flow. In the heated section, five rectangular ribs are positioned on the bottom surface of the channel at regular intervals of $P = 100$ mm, with a consistent height and length of all ribs at $e = 10$ mm; corresponding aspect ratio, P/e, is 10. Fig. 3 illustrates three different rib arrangements without perforations with three different inclination angles (α) of 90°, 60°, and 30°.

Table 2
Thermal and hydraulic performance in Cases 1, 2, and 3.

Case	$\overline{Nu}/\overline{Nu}_0$	f/f_0	η
Case 1	1.272	2.853	0.897
Case 2	1.567	3.810	1.003
Case 3	1.488	2.367	1.117

The boundary conditions were adopted from previous experiments and numerical simulations [17,18,29,30]. In the simulation, we applied a uniform heat flux of q_w =1000 W/m^2 to the heated wall, consistent with the conditions used in the literature [5], whereas all other walls were treated as adiabatic. The inlet fluid was assumed to be incompressible dry air with constant thermal and physical properties, as listed in Table 1. The velocity-inlet boundary condition was set to ensure the inlet flow would enter perpendicular to the wall. The inlet air was set to have a constant temperature of $T_{in} = 300$ K, and a uniform inlet velocity was estimated with a corresponding Reynolds number of 80,000 and a channel hydraulic diameter of 128 mm. The grid-independence tests were performed for Case 1 to determine a suitable mesh system for simulation, as shown in Fig. 4. The static temperature of the air was monitored along line A-A' within the heated section extending from z = 600 mm to z = 1600 mm at x = 160 mm and y = 20 mm. Based on the test results, this study selected mesh structures with 10.9 million elements for Case 1, which exhibited maximum temperature differences of approximately 0.14 K.

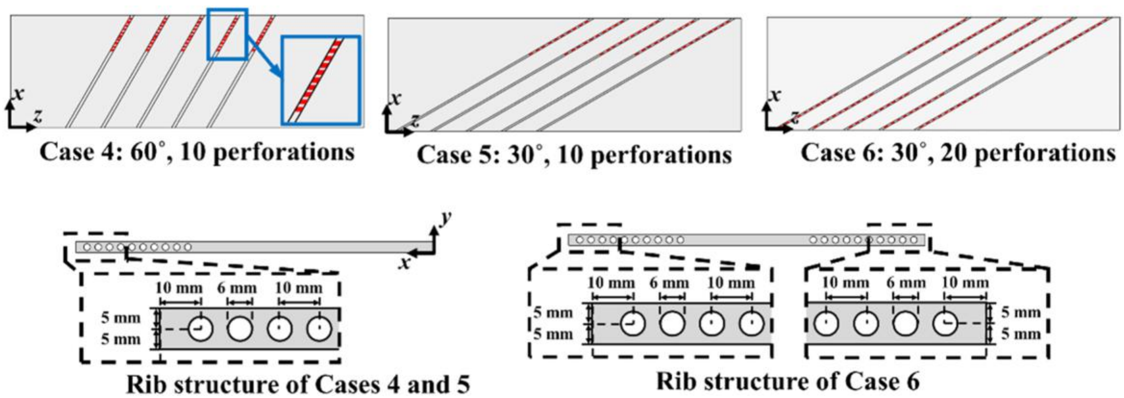

Fig. 9. Configurations of the three different cases with perforations.

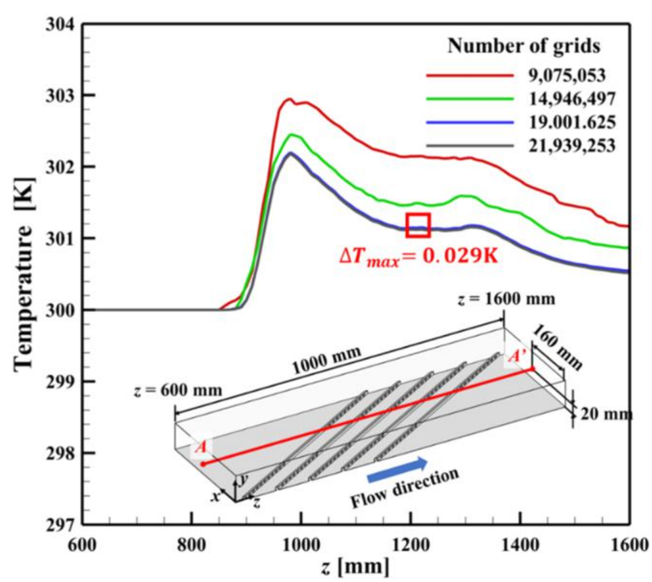

Fig. 10. Grid-independence tests for Case 6.

3. Results and discussion

3.1. Effect of inclination angle on heat transfer characteristics without perforations

The velocity magnitude and streamlines in the y-z plane at $x = 160$ mm for Case 1 are presented in Fig. 5. As the flow passes over the rib, flow separation occurs, creating a recirculation zone. The fluid then reattaches to the wall. A large separation vortex dominates the region between the first and second ribs. Beyond the second rib, the recirculation zone becomes significantly compressed due to reduced flow velocity, and a reattachment zone emerges between the ribs.

The present study analyzed streamlines and Q-criterion isosurfaces to elucidate the effects of different rib structures on flow distributions. The Q-criterion isosurface is a widely used method for vortex visualization, identifying regions where the vorticity magnitude exceeds the strain rate magnitude. Previous studies [31,32] have shown that the appropriate selection of Q-criterion value is essential for accurately capturing vortex regions. The Q-criterion is mathematically defined as

$$Q = \frac{1}{2}\left(\| \Omega \|^2 - \| S \|^2\right), \tag{14}$$

where Ω represents the vorticity, and S denotes the strain rate.

Figs. 6(a) and (b) present the Q-criterion isosurfaces and calculated streamlines for Cases 2 and 3, respectively. The inclined ribs generate asymmetric flow and promote the development of secondary flows along the rib surfaces, generating vortical motion that enhances flow mixing. As the flow moves along the inclined ribs, it interacts with the sidewalls, forming an upward secondary flow that moves away from the bottom surface. Case 3 produces secondary flows that are more uniform and aligned with the mainstream direction because of the influence of the smaller inclination angle compared to Case 2, as shown in Fig. 6(b).

Fig. 7 presents the velocity magnitude distributions on the x–z plane at $y = 1$ mm for Cases 1, 2, and 3. As shown in Fig. 7(a), in Case 1, high velocity is observed within the recirculation zone between the first and second ribs, where reverse flows are mainly present. Beyond the second rib, however, recirculation zones with lower flow velocities occur, and the reattachment zone also enhances local flow mixing. Unlike Case 1, Cases 2 and 3 generate asymmetric flow structures due to the inclined ribs. As shown in Fig. 7(b), in Case 2, the secondary flow near the right end of the rib at $x = 0$ with high velocity occurs, and it rotates along the inclined rib. Lower velocity is also observed at the left end of the rib, where the upward secondary flow takes place and moves away from the bottom surface. Fig. 7(c) illustrates that Case 3 exhibits high velocity in the secondary flow regions; however, the velocity distribution becomes more uniform along the inclined rib owing to the smaller inclination angle of the rib.

Fig. 8 illustrates the normalized Nusselt number distributions on the bottom wall for Cases 1, 2, and 3. In Case 1, a high heat transfer region is observed in the middle area between the ribs, where reattachment flow occurs. Meanwhile, relatively lower convective heat transfer is present behind the ribs due to recirculation flow. In contrast, in cases with inclined ribs, convective heat transfer varies significantly along the rib surfaces because of the asymmetric flow characteristics induced by the inclination. Figs. 8(b) and (c) demonstrate that in Cases 2 and 3, high heat transfer regions develop near the right end of the rib, caused by high-velocity secondary flow, whereas the low heat transfer regions emerge in the upward secondary flow regions near the left end of the rib. Similar to Case 1, low heat transfer regions are also identified behind the ribs due to recirculating flow. These results suggest that high heat transfer regions are predominantly concentrated near the right end of the rib, whereas low heat transfer occurs near the left end of the rib, highlighting the asymmetric nature of the heat transfer.

Table 2 presents the normalized Nusselt numbers, normalized friction losses, and overall thermal performance factors for Cases 1, 2, and 3, calculated using Eqs. (8) to (12). Compared to Case 1, the normalized Nusselt number increases by approximately 23.2 % in Case 2 and 17.0 % in Case 3. Given that strong spanwise vortices are closely associated with higher pressure drop [15], Case 2 exhibits the highest normalized friction losses, whereas Case 3 shows the lowest values. The results indicate that Cases 2 and 3 enhance the overall thermal performance factor relative to Case 1, with increases of 11.9 % and 24.5 %, respectively.

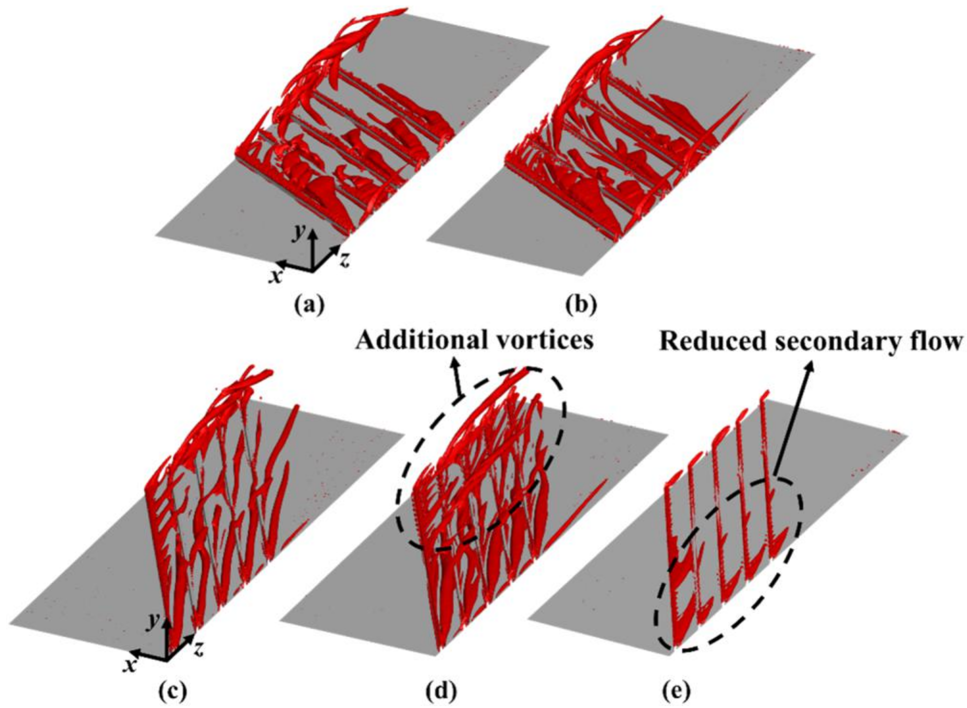

Fig. 11. Q-criterion isosurfaces for visualizing vortical flow structures: (a) no perforations with $\alpha = 60^\circ$ (Case 2), (b) 10 perforations with $\alpha = 60^\circ$ (Case 4), (c) no perforations with $\alpha = 30^\circ$ (Case 3), (d) 10 perforations with $\alpha = 30^\circ$ (Case 5), and (e) a double-perforation rib arrangement with $\alpha = 30^\circ$ (Case 6).

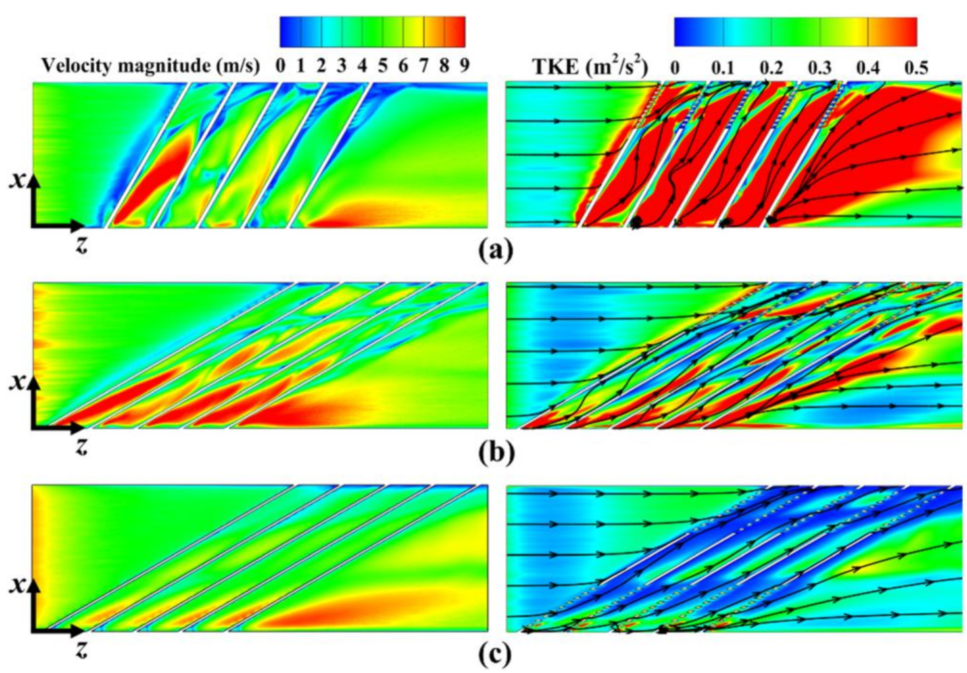

Fig. 12. Contours of velocity magnitude and TKE on the x–z plane (a) Case 4, (b) Case 5, and (c) Case 6.

Case 2 shows the highest normalized Nusselt number, which is accompanied by the most significant friction loss. When considering both pressure loss and heat transfer enhancement, it is found that Case 3 exhibits the highest overall thermal performance among the three cases, indicating the effectiveness of inclined ribs for turbine blade cooling, which is consistent with previous findings [15,16].

3.2. Heat transfer enhancement by tailoring local perforations

Previous studies have reported that localized perforations in rib structures can enhance flow reattachment, mitigate low heat transfer regions, and reduce pressure drop by minimizing flow resistance [17,18,25]. However, as discussed above, the inherent asymmetry in heat transfer distribution induced by inclined ribs suggests that uniformly spaced perforations may not always be advantageous. Thus, the present study aims to propose a rib structure with tailored local perforations to

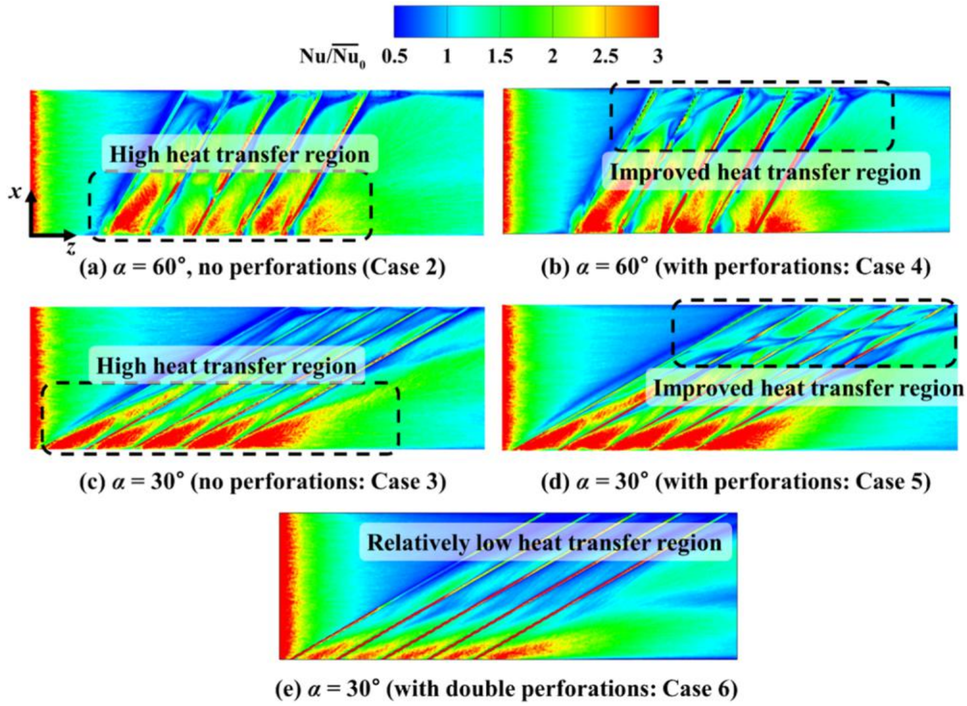

Fig. 13. Normalized Nusselt number distributions at the bottom surface of the heated section.

enhance heat transfer by comprehensively considering the effects of local flow dynamics, asymmetric heat transfer behavior, and secondary flow interactions.

Fig. 9 depicts the perforated rib arrangement on the bottom wall of the heated section. Cases 4 and 5 are designed to investigate the effects of local perforations on heat transfer and pressure drop for inclination angles of 60° and 30°, respectively. In each case, 10 perforations are strategically placed near the left end of the ribs to enhance heat transfer in regions affected by upward secondary flow, as observed in Cases 2 and 3. Ten round holes are incorporated into the ribs, each with a diameter of 6 mm, positioned 5 mm above the bottom surface and spaced 10 mm apart along the z-axis. For comparison, Case 6 has a double-perforation arrangement with 20 perforations, with 10 holes positioned near both ends of the 30° inclined ribs. The hole size and spacing in Case 6 are consistent with those in Cases 4 and 5. Grid-independence test results for Case 6 are presented in Fig. 10. The static temperature of the air was monitored along the A-A' line within the heated section, spanning from $z = 600$ mm to $z = 1600$ mm at $x = 160$ mm and $y = 20$ mm. Based on the results, a grid system consisting of about 19.0 million elements was selected in the present study as it exhibited a temperature deviation of only 0.029 K, ensuring computational accuracy and solution convergence.

Figs. 11(a) and (b) show the Q-criterion isosurfaces for Cases 2 and 4, respectively, to examine the influence of perforations at $\alpha = 60°$ The results indicate no significant differences because the upward secondary vortical flows do not directly interact with the flow ejected from the perforations. In contrast, Figs. 11(c), (d), and (e) illustrate the vortical structures in Cases 3, 5, and 6 at $\alpha = 30°$, demonstrating a pronounced impact of the perforations on the vortical structures. Notably, Case 5 exhibits the generation of additional vortices because of the intensified interaction between the perforation-induced flow and the surrounding secondary vortical flows, compared to Case 3. Meanwhile, Case 6 reveals that the flow discharged from the perforations near the right end of the ribs perturbs the secondary flow regions, expecting a significant change in convective heat transfer. These results provide valuable insight into the correlation between the inclination angle and the perforation effects on vortical structures, which are closely associated with heat transfer enhancement.

Fig. 12 presents the velocity magnitude on the x–z plane at $y = 1$ mm and the TKE distributions with two-dimensional streamlines on the x–z plane at $y = 5$ mm for Cases 4, 5, and 6. Figs. 12(a) and (b) show that the perforations in the inclined ribs increased the velocity near the bottom surface and in regions behind subsequent ribs, where recirculation flow had previously reduced flow velocity. Furthermore, the TKE distributions indicate the presence of vortices induced by the perforations at the rear of the ribs. These velocity enhancements and vortices correspond to improved heat transfer performance, particularly at the end of the ribs. However, Fig. 12(c) shows a significant reduction in velocity and TKE across most regions, including areas previously exhibiting high velocity due to secondary flow. This trend confirms that perforations at the right end of the ribs disrupt the formation of secondary flow, leading to a more simplified overall flow structure. Based on previous results, placing perforations at the left end of the ribs in inclined ribs does not interfere with the high heat transfer regions associated with the secondary flow while improving flow in areas with low heat transfer performance caused by recirculation zones and upward secondary flow. However, perforations at the trailing end of the rib slopes are expected to deteriorate heat transfer performance.

Fig. 13 illustrates the normalized Nusselt number distributions on the bottom wall of the heated section for inclined rib cases. As shown in Figs. 14(a) and (b), a comparison between Case 2 and Case 4 reveals that both configurations exhibit similarly high heat transfer regions at the right end of the rib. However, in the perforated region at the left end of the rib, an increase in the Nusselt number is observed in the low heat transfer zones previously found at the rear of the ribs. Similarly, Figs. 14 (c), (d), and (e) illustrate that Case 5 shows a high heat transfer region near the right end of the rib, similar to Case 3, while also demonstrating improved heat transfer behind the perforations. However, comparison between Cases 5 and 6 shows that the Nusselt number decreases both downstream of the left-end perforations and around the additional perforations near the right ends of the ribs, reducing the overall heat transfer performance.

Fig. 14 compares the heat transfer performance affected by tailored local perforations based on the area-averaged Nusselt number in the

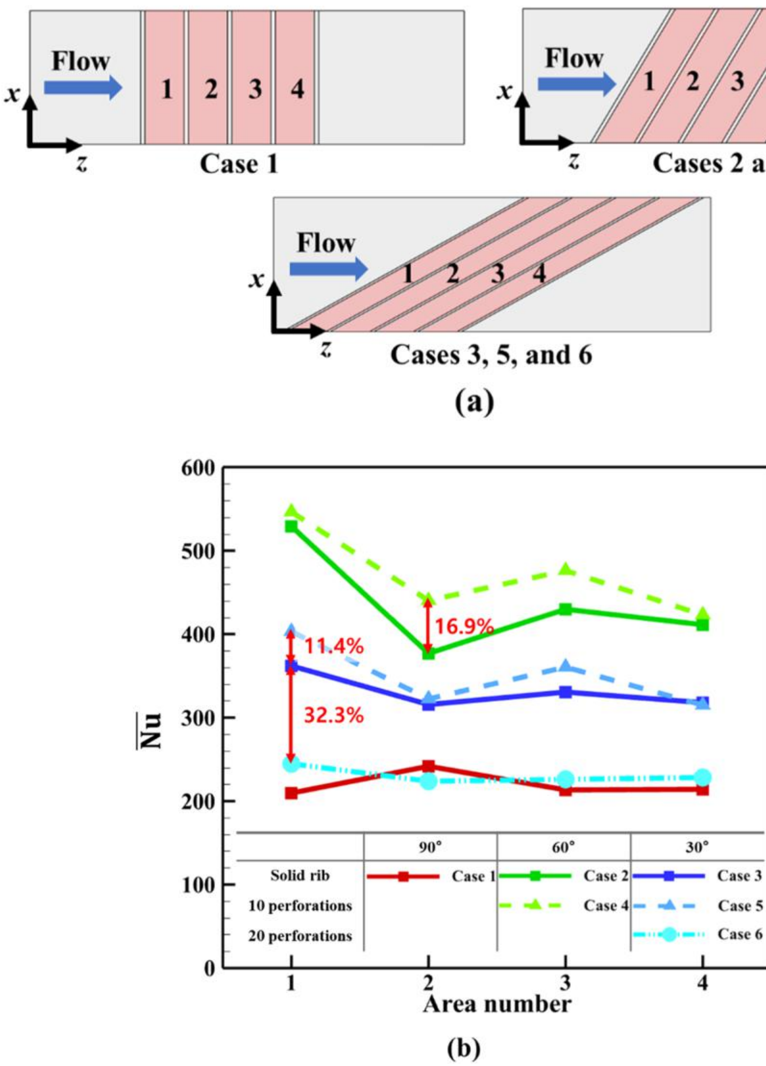

Fig. 14. (a) A schematic of the selected areas and (b) Area-averaged Nusselt numbers.

Table 3
Thermal and hydraulic performance in cases 4, 5, and 6.

Case	$\overline{\mathrm{Nu}}/\overline{\mathrm{Nu}}_0$	f/f_0	η
Case 4	1.647	3.752	1.060
Case 5	1.554	2.233	1.189
Case 6	1.403	2.191	1.080

regions between ribs. Fig. 14(a) illustrates the four selected areas used to calculate the area-averaged Nusselt number between the five ribs by using Eq. (8). As shown in Fig. 14(b), the non-perforated rib cases (Cases 1, 2, and 3) exhibit trends consistent with the normalized Nusselt numbers listed in Table 2. In contrast, Cases 4 and 5 exhibit increased Nusselt numbers across all rib regions, consistent with the previous analysis. The maximum heat transfer enhancements of 16.9 % and 11.4 %, respectively, clearly show that localized perforations can effectively contribute to improving thermal performance. Conversely, Case 6, which contains 20 perforations, shows a reduction of up to 32.3 % in the Nusselt number compared to Case 3 - the corresponding non-perforated rib case inclined at 30°. This result reveals an undesirable effect of excessive perforations on the heat transfer performance of rib structures.

Table 3 presents the normalized Nusselt numbers, normalized friction losses, and overall thermal performance factors for Cases 4, 5, and 6. Fig. 15 also compares the thermal and hydraulic performance across

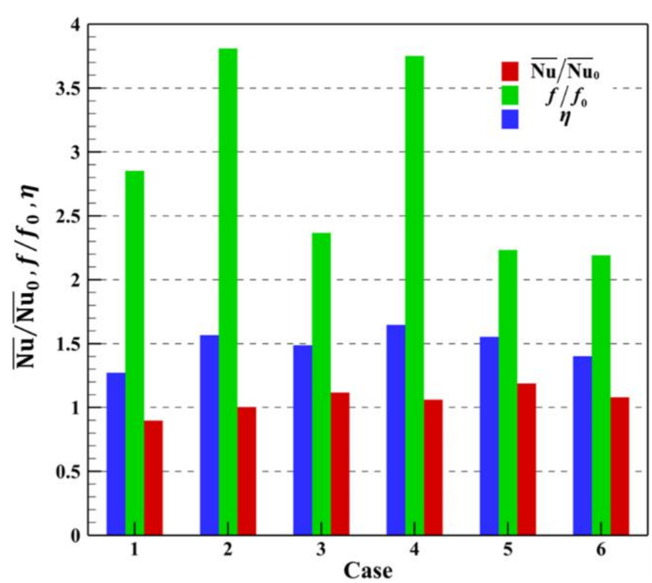

Fig. 15. Comparison of thermal and hydraulic performance across all cases.

all six cases. Similar to the trends observed in Table 2 and Fig. 14(b), the 60° inclined ribs exhibited a higher normalized Nusselt number and higher normalized friction losses than the 30° inclined ribs. Compared to the corresponding non-perforated cases, Case 4 showed a 5.1 % increase in the normalized Nusselt number relative to Case 2, while Case 5 exhibited a 4.5 % increase compared to Case 3. The reduction in flow blockage also decreased normalized friction losses by 1.5 % in Case 4 and 5.7 % in Case 5. Consequently, the application of perforations improved overall thermal performance with increases of 5.7 % in Case 4 and 6.5 % in Case 5, compared to the non-perforated ribs. In contrast, Case 6 showed a 9.7 % decrease in normalized Nusselt number compared to Case 5. Also, the normalized friction loss decreased by 1.9 %, primarily due to the suppression of secondary flows induced by the 10 additional perforations. Thus, the overall thermal performance factor of Case 6, which includes additional perforations, decreased by 3.3 % compared to Case 5, which contains 10 perforations only at the left end of the ribs.

4. Conclusions

The present study demonstrated enhanced heat transfer performance in inclined-rib channels by introducing partial perforations into the inclined ribs. The investigated configurations included non-perforated ribs inclined at 90° (vertical ribs), 60°, and 30°; ribs with 10 perforations inclined at 60° and 30°; and 30° inclined ribs with double perforations. The thermal and flow performance of the ribs was evaluated based on the Nusselt number, friction loss, and overall thermal performance factor. The conclusions are drawn as follows:

1. The inclined rib configurations (60° and 30°) demonstrated higher normalized Nusselt numbers than the 90° rib configuration, attributed to strong secondary flows along the ribs that enhanced heat transfer performance along the channel surface. However, lower local Nusselt numbers were observed behind the ribs due to recirculation flows and at the ends of the ribs due to upward secondary flows. The overall thermal performance factor of the inclined rib configurations was superior to that of the vertical rib configuration, with Cases 2 and 3 showing improvements of 11.9 % and 24.5 %, respectively, compared to Case 1.
2. Perforations at the end of the rib slopes can improve the low heat transfer regions observed in non-perforated inclined rib cases. They generated additional vortices behind the ribs, enhancing heat transfer in areas affected by recirculation and upward secondary flow zones. Results showed that the perforated rib configurations enhanced the overall thermal performance factor relative to the non-perforated rib configurations, with Cases 4 and 5 yielding improvements of 5.6 % and 6.5 %, respectively.
3. The 30° inclined rib configuration with 20 perforations showed a lower normalized friction loss due to reduced blockage. However, additional perforations at the right end of the rib slopes suppressed the formation of secondary flow, leading to a lower normalized Nusselt number. As a result, the overall thermal performance factor of Case 6 showed a 3.3 % reduction compared to Case 5, indicating a decrease in thermal efficiency. Therefore, the results indicate that the optimal design is Case 5, with ten perforations applied at the left end of the ribs, which are inclined at 30°

It is noted that in real-world applications, various design factors could affect heat transfer in rib turbulators. In particular, the aspect ratio of the channel wall is one of the key factors closely associated with heat transfer and flow characteristics due to side wall effects. Therefore, future work will focus on investigating the influence of channel aspect ratio on the performance of inclined and perforated ribs.

CRediT authorship contribution statement

Dosang Lee: Writing – original draft, Visualization, Validation, Software, Methodology, Investigation, Formal analysis, Data curation, Conceptualization. **Hyung Ju Lee:** Writing – review & editing, Validation, Methodology, Investigation. **Hyoungsoon Lee:** Writing – review & editing, Validation, Methodology, Investigation. **Seong Hyuk Lee:** Writing – review & editing, Validation, Supervision, Resources, Project administration, Investigation, Funding acquisition, Formal analysis, Conceptualization.

Declaration of competing interest

The authors declare the following financial interests/personal relationships which may be considered as potential competing interests:

Seong Hyuk Lee reports financial support was provided by Korea Ministry of Science and ICT. Dosang Lee reports financial support was provided by Chung-Ang University. Seong Hyuk Lee reports financial support was provided by National Research Foundation of Korea. If there are other authors, they declare that they have no known competing financial interests or personal relationships that could have appeared to influence the work reported in this paper.

Acknowledgements

This research was supported by the Chung-Ang University Graduate Research Scholarship in 2024. Also, this work was supported by the National Research Foundation of Korea (NRF) grant funded by the Korea government (MSIT) (No.NRF-2021R1A2C3014510). Moreover, this work was supported by the IITP(Institute of Information & Communications Technology Planning & Evaluation)-ITRC(Information Technology Research Center) grant funded by the Korea government (Ministry of Science and ICT) (IITP-RS-2024-00436248, 20 %).

Data availability

Data will be made available on request.

References

[1] Terzis, A., (2014). Detailed heat transfer distributions of narrow impingement channels for integrally cast turbine airfoils, in, EPFL.

[2] J.-C. Han, S. Dutta, S. Ekkad, Gas Turbine Heat Transfer and Cooling Technology, CRC press, 2012.

[3] J.-C. Han, Advanced cooling in gas turbines 2016 Max Jakob memorial award paper, J. Heat Transf. 140 (2018) 113001.

[4] L.M. Wright, J.-C. Han, Enhanced internal cooling of turbine blades and vanes, Gas Turbine Handb. 4 (2006) 1–5.

[5] S.-F. Zheng, G.-Q. Liu, Y. Zhang, H.-C. Wang, S.-R. Gao, Y.-R. Yang, H.-W. Li, B. Sunden, X.-D. Wang, Performance evaluation with turbulent flow and heat transfer characteristics in rectangular cooling channels with various novel hierarchical rib schemes, Int. J. Heat Mass. Transf. 214 (2023) 124459.

[6] J. Ahn, Large Eddy simulation of flow and heat transfer in a ribbed channel for the internal cooling passage of a gas turbine blade: a review, Energies 16 (2023) 3656.

[7] Y. Mahanand, J.R. Senapati, Implementation of hybrid rib-turbulators on the thermal performance of solar air heater duct: a collective review, Sustain. Energy Technol. Assess. 52 (2022) 102345.

[8] S. Ran, P. Zhang, Y. Rao, Numerical study of heat transfer and flow structure over channel surfaces featuring miniature V rib-dimples with various configurations, Int. J. Therm. Sci. 172 (2022) 107342.

[9] E.Y. Choi, Y.D. Choi, W.S. Lee, J.T. Chung, J.S. Kwak, Heat transfer augmentation using a rib–dimple compound cooling technique, Appl. Therm. Eng. 51 (2013) 435–441.

[10] C. Liang, Y. Rao, J. Luo, X. Luo, Experimental and numerical study of turbulent flow and heat transfer in a wedge-shaped Channel with guiding pin fins for turbine blade trailing edge cooling, Int. J. Heat Mass Transf. 178 (2021) 121590.

[11] W. Jin, J. Wu, N. Jia, J. Lei, W. Ji, G. Xie, Effect of shape and distribution of pin-fins on the flow and heat transfer characteristics in the rectangular cooling channel, Int. J. Therm. Sci. 161 (2021) 106758.

[12] A.R. Salem, F.N. Nourin, M. Abousabae, R.S. Amano, Experimental and numerical study of jet impingement cooling for improved gas turbine blade internal cooling with in-line and staggered nozzle arrays, J. Energy Resour. Technol. 143 (2021) 012103.

[13] A. Safi, M.O. Hamdan, E. Elnajjar, Numerical investigation on the effect of rotation on impingement cooling of the gas turbine leading edge, Alex. Eng. J. 59 (2020) 3781–3797.
[14] E. Kianpour, N.A.C. Sidik, I. Golshokouh, Film cooling effectiveness in a gas turbine engine: a review, J. Teknol. 71 (2014) 25–35.
[15] N. Kaewchoothong, K. Maliwan, K. Takeishi, C. Nuntadusit, Effect of inclined ribs on heat transfer coefficient in stationary square channel, Theor. Appl. Mech. Lett. 7 (2017) 344–350.
[16] B. Yang, T. Gao, J. Gong, J. Li, Numerical investigation on flow and heat transfer of pulsating flow in various ribbed channels, Appl. Therm. Eng. 145 (2018) 576–589.
[17] J. Liu, S. Hussain, W. Wang, L. Wang, G. Xie, B. Sundén, Heat transfer enhancement and turbulent flow in a rectangular channel using perforated ribs with inclined holes, J. Heat Transf. 141 (2019) 041702.
[18] J. Liu, S. Hussain, W. Wang, G. Xie, B. Sundén, Experimental and numerical investigations of heat transfer and fluid flow in a rectangular channel with perforated ribs, Int. Commun. Heat Mass Transf. 121 (2021) 105083.
[19] W. Qian, R. Shuai, Q. Meng, S. Roy, S. Yao, P. Wang, Mechanistic insights into effects of perforation direction on thermal hydraulic performance of ribs in a rectangular cooling channel, Aerospace 11 (2024) 675.
[20] D.H. Kim, B.J. Lee, J.S. Park, J.S. Kwak, J.T. Chung, Effects of inlet velocity profile on flow and heat transfer in the entrance region of a ribbed channel, Int J Heat Mass. Transf. 92 (2016) 838–849.
[21] T. Gao, J. Zhu, C. Liu, J. Xu, Numerical study of conjugate heat transfer of steam and air in high aspect ratio rectangular ribbed cooling channel, J. Mech. Sci. Technol. 30 (2016) 1431–1442.
[22] N. Sharma, A. Tariq, M. Mishra, Detailed heat transfer and fluid flow investigation in a rectangular duct with truncated prismatic ribs, Exp. Therm. Fluid Sci. 96 (2018) 383–396.
[23] L. Marocco, A. Franco, Direct Numerical Simulation and RANS comparison of turbulent convective heat transfer in a staggered ribbed channel with high blockage, J. Heat Transf. 139 (2017) 021701.
[24] A. Keshmiri, J. Gotts, Thermalhydraulic analysis of four geometrical design parameters in rib-roughened channels, Numer. Heat Transf. A.: Appl. 60 (2011) 305–327.
[25] S. Javanmard, A. Ashrafizadeh, A comparative numerical study on heat transfer and pressure drop characteristics of perforated ribs, Int. J. Therm. Sci. 191 (2023) 108373.
[26] X. Li, G. Xie, J. Liu, B. Sunden, Parametric study on flow characteristics and heat transfer in rectangular channels with strip slits in ribs on one wall, Int. J. Heat Mass Transf. 149 (2020) 118396.
[27] S.-F. Zheng, W.-K. Lian, J.-X. Meng, H.-C. Wang, S.-R. Gao, Y.-R. Yang, H.-W. Li, B. Sunden, X.-D. Wang, An inverse optimization of turbulent flow and heat transfer for a cooling passage with hierarchically arranged ribs in turbine blades, Int. J. Heat Mass. Transf. 220 (2024) 124961.
[28] I. Ansys, Ansys Fluent 2020 R2 User's Manual, ANSYS Inc, 2020.
[29] J. Liu, S. Hussain, J. Wang, L. Wang, G. Xie, B. Sundén, Heat transfer enhancement and turbulent flow in a high aspect ratio channel (4: 1) with ribs of various truncation types and arrangements, Int. J. Therm. Sci. 123 (2018) 99–116.
[30] S. Alfarawi, S. Abdel-Moneim, A. Bodalal, Experimental investigations of heat transfer enhancement from rectangular duct roughened by hybrid ribs, Int. J. Therm. Sci. 118 (2017) 123–138.
[31] Y. Dubief, F. Delcayre, On coherent-vortex identification in turbulence, J. Turbul. 1 (2000) 011.
[32] C. Liu, Y.-S. Gao, X.-R. Dong, Y.-Q. Wang, J.-M. Liu, Y.-N. Zhang, X.-S. Cai, N. Gui, Third generation of vortex identification methods: omega and Liutex/Rortex based systems, J. Hydrodyn. 31 (2019) 205–223.